ISABE-2011-1717

Low-Pressure Turbine End Wall Design Optimisation and Experimental Verification in the Presence of Purge Flow

P. Jenny[1], R.S. Abhari[1], M.G. Rose[2], M.Brettschneider[3], J.Gier[3], K.Engel[3]

[1] Laboratory for Energy Conversion, Department of Mechanical and Process Engineering, ETH Zurich, Switzerland
[2] Institute of Aeronautical Propulsion, University of Stuttgart, 70569 Stuttgart, Germany
[3] MTU Aero Engines GmbH, Dachauer Strasse 665, 80995 Munich, Germany

Abstract

In this paper the effect of non-axisymmetric end wall contouring in a shrouded low-pressure turbine rotor in the presence of purge flow is analysed. In particular, the combined effects of profiled end walls and injected purge flow are studied. Probe measurements were taken at the inlet and the exit of three different shrouded turbine rotors. Two rotors have profiled end walls at hub and tip, designed using an automatic numerical optimisation based on an in-house MTU code. For each of the rotor geometries several levels of purge flow were considered providing a consistent and complete data matrix for the study. For the operating point under investigation two of the tested rotors have pressure side separations. The 2-sensor Fast Response Aerodynamic Probe (FRAP) technique developed at ETH Zurich is used in this experimental campaign. Time-resolved measurements of the unsteady pressure and temperature between the rotor and stator blade rows are taken. In addition, the results of unsteady RANS simulations are compared to the measurements and the computations are also used to detail the flow field. The design of the non-axisymmetric end walls showed the beneficial effects of improved measured efficiency at this operating point, together with a reduced sensitivity to purge flow.

Nomenclature

m	mass flow	[kg/s]
p	pressure	[Pa]
$\bar{p}$	time mean part of pressure signal	[Pa]
$\tilde{p}$	periodic part of pressure signal	[Pa]
p'	random part of pressure signal	[Pa]
T	temperature	[K]
Re	Reynolds number	[-]
IR	injection rate	[%]
N	rotational speed	[rpm]
M	torque	[Nm]
t	time	[s]
U	rotational speed	[m/s]
C_P	specific heat capacity	[J/kg/K]
η	efficiency	[-]
Π	pressure ratio	[-]
γ	isentropic coefficient	[-]
Ω	vorticity	[1/s]

Subscripts

t	stagnation flow quantity
s	static flow quantity
rel	relative frame flow quantity
tt	total-to-total
in	turbine inlet flow quantity
S	streamwise

Abbreviations

FRAP	Fast Response Aerodynamic Probe
rms	root mean square
NGV1	first nozzle guide vane
NGV2	second nozzle guide vane
R1	rotor 1
R1ex	rotor 1 exit
S1	stator 1
S1ex	stator1 exit
S2	stator 2
CFD	computational fluid dynamics

Introduction

The purge flow injected at the rim seal between the nozzle guide vane and rotor is the secondary cooling mass flow considered for this work. The purge flow is bypassed compressor air and prevents the ingestion of hot gases into the disk cavities in

order to prevent rotor disk overheating and to avoid thermal fatigue. The ingestion of hot gases is driven by disk pumping and the external non-axisymmetric static pressure field. This has been experimentally investigated in previous studies. Chew et al. [1] and Dadkhah et al. [2] analysed the minimum required coolant flow for different rim seal shapes and compared this to the differential pressure criterion. Kobayashi et al. [3] found that the pressure difference criterion underestimated the minimum cooling flow rate. The strong effect of injected cooling air on the development of the secondary flow structures has been reported in the open literature. McLean et al. [4] experimentally found the three-dimensional secondary flow structure and stage performance to be significantly affected by the cooling mass flow. Ong et al. [5] reported that the introduction of a swirl component to the coolant jet reduces the efficiency penalty caused by the coolant due to a reduction in viscous dissipation and secondary flow strength. Furthermore, they found that most of the coolant is entrained by the downstream blade hub secondary flow. Paniagua et al. [6] found that there is an intensification of the rotor hub vortex and an enhancement of the radial migration due to injection in a transonic high pressure turbine. Reid et al. [7] quantified the efficiency penalty caused by the rim seal flow as being about 0.56% per percent of injection mass flow. Schuepbach et al. [8] have shown a 0.6% efficiency drop for 0.9% purge flow with axisymmetric end walls. Additionally, intensification of the secondary flows at the exit of the rotor as well as a higher penetration of the secondary flows with purge flow were observed.

Gilbert Riollet [9], in his 1965 patent, published the generic geometry of non-axisymmetric end wall profiling for the first time. In the axial flow gas turbine context, 30 years later such end walls were first proposed and designed by Rose [10] with the benefit of 3D CFD. The profiled end walls were initially designed to homogenise the end wall static pressure field at the rim seal, with the aim of reducing the required turbine disk coolant mass flow. Later Hartland et al. [11] and Ingram et al. [12] showed in the Durham linear cascade that significant secondary loss reductions can be achieved using non-axisymmetric end walls. Brennan et al. [13] and Rose et al. [14] redesigned the end walls of an HP turbine model rig and reported an increase in stage efficiency of 0.4% from computations and 0.6% ±0.25% from measurements. Praisner et al. [15] have confirmed that end wall contouring is an effective method for reducing end wall losses in a high-lift airfoil cascade using a CFD-based end wall optimiser. Schuepbach et al. [16] performed measurements with the model axial turbine test rig used for the current experimental measurement campaign and reported an efficiency improvement of 1.0%±0.4% due to the non-axisymmetric nozzle guide vane and rotor end walls designed by Germain et al. [17].

For cost reasons in most applications low-pressure turbine blades are thin and solid. Because of their small leading edge radius low-pressure turbine blades often have separated flow on the pressure side. The behaviour of the separation bubble is complex and highly unsteady. Brear et al. [18] quantified the loss produced by a pressure side bubble in a linear cascade, showing that it can be a significant contributor to the profile loss. They also found the incidence to be the controlling parameter for the characteristics of the pressure side separation. Similar findings were reported by Yamamoto et al. [19] and Hodson et al. [20]. The migration process of the separated fluid was first studied by Brear et al. [21] who proposed a strong interaction with the hub secondary flows.

This paper experimentally quantifies the combined flow interaction mechanisms between purge flow, profiled end walls and a separated pressure side. The profiled end walls were designed to mitigate the effect of purge flow. Three shrouded low-pressure rotor geometries are tested in a model axial turbine. The time-resolved measurements are made in a rotating model axial turbine and compared to the results of a high-fidelity numerical model.

Experimental Method

The experimental investigation was performed in the "LISA" research turbine at the Laboratory for Energy Conversion (LEC) at the Swiss Federal Institute of Technology in Zurich (ETH).

Experimental Turbine Facility

The air loop of the facility is quasi-closed and includes a radial compressor, a two-stage water to air heat exchanger and a calibrated venturi nozzle for mass flow measurements. Upstream of the turbine section is a 3m flow conditioning stretch to ensure a homogenous flow field. Additionally, the flow undergoes acceleration ahead of the turbine section in order to reduce the significance of remaining flow non-uniformities from upstream. At the exit of the turbine section the air loop opens to the atmosphere. A DC generator absorbs the turbine power and controls the rotational speed with an accuracy of ±0.02% (±0.5RPM). A heat exchanger controls the inlet total temperature $T_{t,in}$ to an accuracy of ±0.3%. A torquemeter measures the torque on the rotor shaft. With the compressor ratio limited to $\Pi_{c,max}$=1.4 it is

necessary to add a tandem de-swirl vane arrangement to bring the static pressure at the exit of the second stator back to the ambient level, in order to reach the intended turbine total-to-static pressure ratio of $\Pi_{1.5}$ = 1.65. At the exit of the first nozzle guide vane row the flow is compressible with an exit Mach number of 0.53.

$\Pi_{1.5}$	$1.65 \pm 0.4\%$	$[-]$
$T_{t,in}$	328 ± 0.2	$[K]$
$\frac{\dot{m}\sqrt{T_{t,in}}}{p_{t,in}}$	$152 \pm 0.2\%$	$\left[\frac{kg \cdot \sqrt{K}}{s \cdot bar}\right]$
$\frac{N}{\sqrt{T_{t,in}}}$	2.48 ± 0.05	$\left[\frac{r.p.s.}{K^{1/2}}\right]$
Mach (S1ex/R1ex/S2ex)	0.52/0.28/0.48	$[-]$
Re (S1/R1/S2)	$7.1/3.8/5.1 \cdot 10^5$	$[-]$
Blade count (S1/R1/S2)	36/54/36	$[-]$
Aspect ratio (S1/R1/S2)	0.87/1.17/0.82	$[-]$

Table 1. Operating conditions and geometrical characteristics.

Operating Conditions

During all measurements the turbine 1.5 stage total-to-static pressure ratio is kept constant at $\Pi_{1.5}$ = 1.65 and the total turbine entry temperature is kept uniform at $T_{t,in}$ = 328K. In order to account for the change in ambient pressure on different measurement days, the pressures are non-dimensionalised by the respective inlet total pressure. These operating conditions are in agreement with measurements previously obtained using this turbine and permit an accurate comparison between measurements made on different days.

Injection System

The air injected through the rim seal between the nozzle guide vane and rotor is bled off the primary air-loop upstream of the main flow conditioning stretch. The mass flow of the bypassed air is measured by means of a venturi, which is part of the auxiliary air system. After having passed a plenum, the air is fed into the rim seal cavity through tunnels inside 10 different nozzle guide vanes, labelled B in Figure 1, which illustrates the leakage path and the rim seal cavity. From the cavity underneath the nozzle guide vanes there are two leakage paths, which are indicated in Figure 1 as dotted arrows P and S. One path is through the upstream rim seal into the main flow, P. The rest of the gas, called the secondary mass flow S, is ejected through the drum to ambient conditions after being measured in another venturi. The pressure difference over the labyrinth seal between the downstream rim seal and the drum is balanced. Under these conditions the net mass flow through the downstream rim seal into the drum is assumed to be zero.

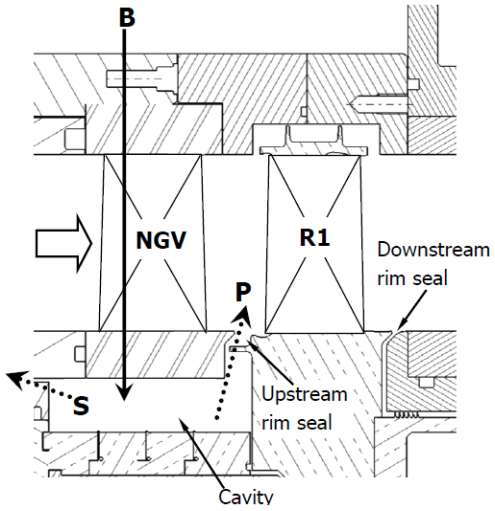

Figure 1. Illustration of leakage path.

Thus the injected mass flow can be calculated as the difference between the measured bypass and the secondary mass flows. The injection rate (IR) is defined as the ratio between the injected mass flow and the total turbine mass flow, given by Equation 1.

$$IR = \frac{\dot{m}_{bypass} - \dot{m}_{drum}}{\dot{m}_{main}} \cdot 100 \tag{1}$$

The measurements were conducted with the following three different injection rates: IR = 0.4%, IR = 0.8% and IR = 1.2%, which are representative of low, nominal and high injection rates.

Measurement Planes

The data was measured at two different traversing planes in the turbine test facility. The first traversing plane (S1ex) is between the first nozzle guide vane and the rotor. The second measurement plane (R1ex) is at the exit of the rotor, upstream of stator two. At traverse planes S1ex and R1ex the spatial resolution of the measurement grid consisted of 42 radial and 41 equally spaced points in the circumferential direction covering one stator pitch. The measurement grid shows radial clustering near the end walls.

Measurement Technology

The unsteady flow field was measured using a standard FRAP developed at ETH Zurich (Kupferschmied et al. [22] and Pfau et al. [23]). It is

capable of capturing unsteady flow features up to frequencies of 48 kHz, based on measurements including total and static pressures, flow yaw and pitch angles and Mach number. The frequency bandwidth of the temperature is limited to a frequency of 10Hz. However, the influence of the measured temperature on the velocity is very modest. The standard FRAP probe has a 1.8mm tip diameter and is equipped with two sensors. The probe is operated in a virtual 4-sensor mode to measure 3-dimensional, time-resolved flow properties. Table 2 gives the relative measurement uncertainties of the FRAP probe as a percentage of the calibration range of ±24° for the yaw angle, ±20° for the pitch angle and as a percentage of the dynamic head for the total and static pressure.

Yaw angle	Pitch angle	P_t	P_s
0.8%	2.3%	1.0%	1.2%

Table 2. Relative uncertainty of the FRAP probe.

The data is acquired at a sampling rate of 200 kHz over a period of 2 seconds. The post-processing is done for three consecutive rotor pitches. The sampling rate resolves 82 points per rotor pitch. During these 2 seconds the three blade passing events are phase-lock-averaged 85 times.

Time-Resolved Computational Model

In parallel to the experiments, corresponding URANS simulations were performed for all test cases using the commercial ANSYS CFX Version 12.1 software package.

The grid used for the time-resolved simulations is structured and has a total of 18.5 million nodes. As the blade count ratio between stationary and rotating blade rows is two to three, two vane passages of the first and second vane rows, as well as three rotor passages, are represented in the mesh with periodic boundary conditions in the circumferential direction. In order to have a realistic rim seal flow field, the cavity space of the test rig configuration between rotor disk and first vane row is fully modelled with an interface to the first NGV exit hub end wall (Figure 1). The non-dimensionalised wall distances on the airfoils and the end walls are on average y+ = 1.5. At the inlet of the turbine domain a constant total pressure and total temperature corresponding to the measured experimental operating conditions were applied. At the exit the measured mass flow under these inlet conditions was imposed as a boundary condition. The purge mass flow rate, measured static pressure and temperature were imposed as boundary conditions at the cavity inlet.

The results of a steady run were used as initial conditions for the time-resolved simulation. The temporal resolution is 80 time steps per period, corresponding to three rotor blade passing events, or a 0.25° shift of the rotor per time step. The shear stress transport (SST) turbulence model without transition modelling was used for the simulations. The maximum residuals were found to be of the order of 10^{-3}, while the mass imbalances were of the order of 10^{-5}. The periodic convergence of the unsteady simulations was judged based on the correlation coefficient of two pressure monitoring points at the rotor exit. Two consecutive vane passage pressure events had to reach a correlation coefficient of over 99%. The time-resolved numerical simulations were validated with the measurements. The time-resolved CFD data offers a close comparison to the experimental results. Quantitative details can be found in Jenny et al. [24].

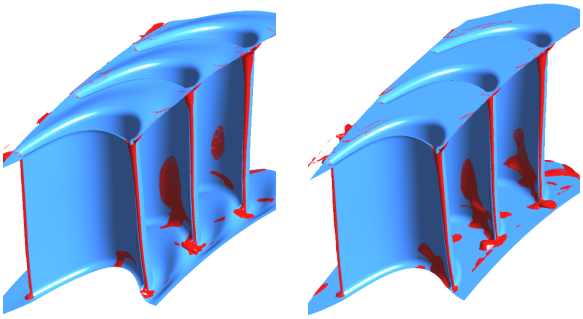

(a) Rotor B (b) Rotor C

Figure 2. Computed iso-surfaces of zero axial velocity for rotors B and C at a specific time step.

Rotor Designs

In the experimental campaign presented three different shrouded rotors were considered. All three rotors have thin airfoils and are representative of a low-pressure rotor:

- **Rotor A** with profiled end walls at hub and tip. This is the baseline rotor.
- **Rotor B** with the same end wall profiling geometry at hub and tip as rotor A but with thinner airfoils below 50% span.
- **Rotor C** with the same blade geometry as rotor B, but with cylindrical end walls.

The two stationary blade rows and their relative position were identical for the measurements with all three rotor designs. For the operating point under investigation the blades of rotors B and C have

pressure side separations. The unsteady behaviour of the pressure side bubble of rotor B was studied by Jenny et al. [24]. Figure 2 is a typical result of the URANS simulations performed in parallel to the experiments, showing iso-surfaces of zero axial velocity on three rotor blades for rotors B and C at one simulated time step. The simulation predicts a pressure side separation in the lower half of the span for both rotor geometries. The modified blade geometry of rotor A suppresses the pressure side bubble.

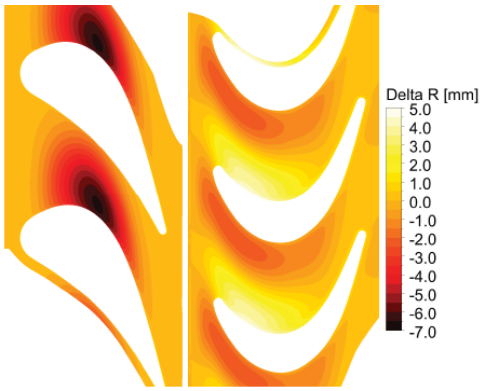

(a) NGV1 and rotor hub end walls

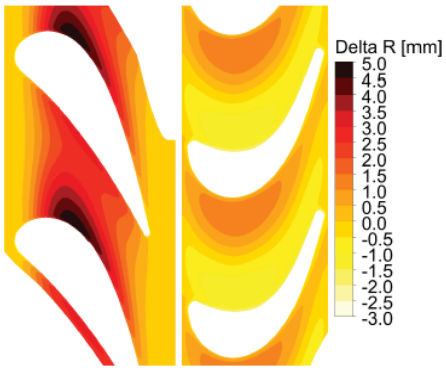

(b) NGV1 and rotor tip end walls

Figure 3. Non-axisymmetric hub and tip end wall shapes from the optimisation.

End Wall and Airfoil Design Methodology

In the experimental campaign the nozzle guide vane has shaped end walls. The main features and the methodology of the corresponding end wall design have been presented by Germain et al. [17]. The primary objectives of the nozzle guide vane end wall optimisation are to reduce secondary kinetic energy and to improve row efficiency. The modified secondary kinetic energy definition is presented in Germain et al. [25]. The rotor end wall contour design of rotors A and B is the result of a three-dimensional end wall optimisation algorithm taking into account purge flow as well as the rim seal and the rotor shroud cavity geometries. The optimisation was performed for nominal operating conditions with a nominal purge flow rate of 0.8% of the main mass flow. A constant flow capacity was imposed as a boundary condition for the optimiser. Rotor tip and hub end walls have been designed using automatic numerical optimisation by means of a gradient-based MTU-in-house optimiser code, the flow being computed by the steady 3D RANS solver TRACE developed at DLR and MTU. The aim of the rotor end wall design was to mitigate the effect of purge flow and to reduce the secondary losses and secondary kinetic energy. The optimiser modified the end wall shape up to the rotor hub platform leading edge and not only between the leading and trailing edges. The result of the end wall profiling optimisation is shown in Figure 3 for the NGV and rotor hub and tip end walls. The NGV hub end wall has a typical suction side trough and higher amplitudes compared to the corresponding rotor hub and tip end walls. The amplitudes at the rotor tip must remain within the thickness of the rotor shroud. The profiling at the rotor hub platform goes up to the leading edge, giving it a wavy shape.

Results and Discussion

In the following section the time-resolved flow field data are presented with particular attention to the unsteady interaction mechanisms between purge flow and end wall profiling. The analysis starts with a discussion of the measurement results at rotor exit for three different injection rates. Corresponding CFD simulations complement the analysis by providing information on the rotor flow field at locations that are inaccessible for the probe measurement technique used.

Effect of end wall profiling on efficiency

The definition of the total-to-total efficiency accounting for the injection used in this study is given in Equation 2:

$$\eta_{tt} = \frac{\frac{\omega M}{\dot{m} C_p T_{t,in}}}{1 - \left(1 - \frac{IR}{100}\right)\left(\frac{p_{t,R1ex}}{p_{t,in}}\right)^{\frac{\gamma-1}{\gamma}} - \frac{IR}{100}\left(\frac{p_{t,R1ex}}{p_{t,cavity}}\right)^{\frac{\gamma-1}{\gamma}}} \quad (2)$$

Figure 4 shows the measured normalised total-to-total efficiency as a function of injected purge flow for rotor geometries A, B and C. Pneumatic probe measurements at the rotor exit are considered. Due to the beneficial effect of shaped end walls on rotor B, the measured total-to-total efficiency has increased by 0.75% for the nominal injection rate on an

absolute scale compared to rotor C with the same blade geometry but cylindrical end walls. Schuepbach et al. [8] reported a 0.3% total-to-total efficiency increase due to successful rotor end wall contouring using the same NGV as in the present experiment but an unshrouded rotor with high pressure turbine representative airfoils. Rotors B and C operate with a pressure side separation in the hub region. The thicker airfoils in the hub region of baseline rotor A operating without pressure side separation further improve the total-to-total efficiency by 0.3% resulting in a total efficiency benefit between rotors A and C of 1.05% at the nominal injection rate.

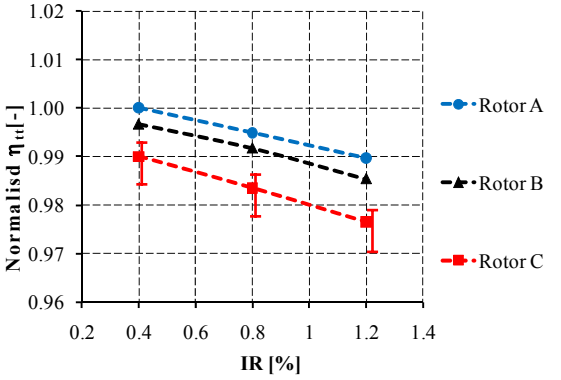

Figure 4. Normalised total-to-total efficiency as a function of injected purge flow with error estimation for rotor C (analogue for rotors A and B).

Sensitivity of Efficiency to Purge Flow

In this section, the effect of injected purge flow on efficiency is analysed for the three rotor geometries. The decrease in efficiency with increasing IR appears to be linear for all three measured rotor geometries. Neither the end wall profiling nor the pressure side separation have an influence on the linear behaviour of the sensitivity to purge flow. For baseline rotor A, the total-to-total efficiency decreases by 1.15% per percent of injected purge flow. The addition of a pressure side bubble due to slimmer airfoils (rotor B) increased this sensitivity to purge flow by 10%. If the end wall profiling is removed at constant blade geometry (rotor C), the sensitivity is further increased to 1.55% efficiency reduction per percent of injected purge flow, resulting in an overall increase of the sensitivity to purge flow of about 32%. Schuepbach et al. [16] reported a 1.2% decrease of total-to-total efficiency per percent of injected fluid. They also reported similar trends for the sensitivity reduction of efficiency to purge flow. Generally speaking, the end wall profiling can bring back the efficiency deficit of about 0.6% of additional purge flow. The combined effect of pressure side bubble suppression and end wall profiling accounts for about 0.8% of injected purge flow.

Interaction Mechanisms between Purge and Secondary Flows

The injected purge flow interacts unsteadily with the main flow and its related secondary flow structures when it is injected and convected down the rotor blade row. The nature of the interaction mechanisms is influenced by the rotor end wall and blade geometries and the amount of injected flow. An interesting parameter to analyse this unsteady interaction with the purge flow is the experimentally evaluated root mean square values (rms) of the random part of the total pressure signal. The unsteady pressure signal provided by the FRAP is considered. Regions of high rms are indicative of significant nondeterministic unsteadiness. This may be due to flow instability modes e.g. eddy shedding or transition or may be simply due to high turbulence. Using the triple decomposition of the time-resolved pressure signal as shown in Equation 3, the random part p'(t) can be evaluated as the difference between the raw pressure signal p(t) of the FRAP and the phase-locked averaged pressure $\bar{p} + \tilde{p}(t)$.

$$p(t) = \bar{p} + \tilde{p}(t) + p'(t) \qquad (3)$$

Figure 5 shows the experimental time-averaged rms distribution of the random part of the total pressure in the rotor frame of reference at the nominal injection rate for rotor B. The plot covers two rotor pitches. The significant high rms feature between 20% to 50% span (zone 1) is the signature of the hub passage vortex. The second high rms feature at about 75% span (zone 2) is caused by the tip passage vortex. The zone of increased rms between the hub and tip passage vortices (zone 3) represents the rotor wake. The elevated rms zone in the tip region over the whole circumference (zone 4) is indicative of fluid leaving the shroud cavity. Figure 5 is representative of all corresponding measurements for the nine investigated test cases (three injection rates versus three rotor geometries). The main difference between these area plots is the rms signature of the hub passage vortex (zone 1). The other flow features (zones 2 to 4) and the free stream region between the rotor wakes appear to be little affected by the level of purge flow and the rotor geometry (cf. Figure 8).

Figure 6 compares the measured peak rms of the $P_{t,rel}$ in the hub loss core at the rotor exit for all test cases investigated. The baseline, rotor A shows the

lowest nondeterministic unsteadiness (1650 Pa) in the hub passage vortex core when compared to rotors B and C for all injection rates. The pressure side separation present for rotor B with the same end wall profiling increases the maximum experimental rms by an average of 25%. When the end wall profiling is removed (rotor C), the peak rms increases by 60% compared to the baseline and by 30% compared to rotor B. In other words, the beneficial effects of the end wall profiling and the removal of the bubble have about the same positive impact on experimental peak rms in the hub loss core for all measured injection rates.

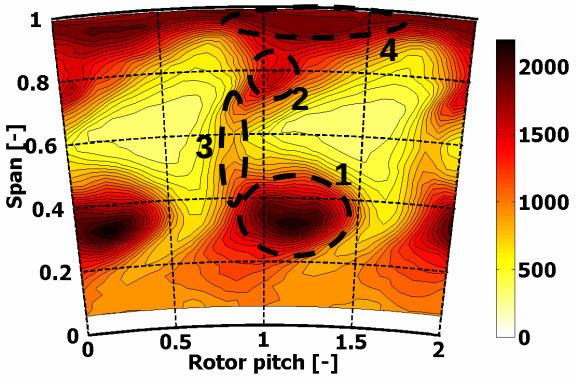

Figure 5. Time-averaged area plot in rotor relative frame of reference at rotor exit for rotor B at the nominal injection rate. The parameter is the experimental rms of the rotor relative total pressure $P_{t,rel}$ [Pa].

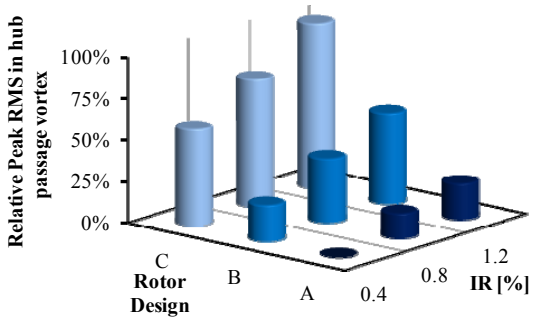

Figure 6. The bars indicate relative increase of peak rms of the rotor relative total pressure $P_{t,rel}$ in the hub passage vortex with reference to the baseline rotor A at the minimum injection rate. The figure compares measurements from all nine test cases investigated (3 injection rates versus 3 rotor geometries) at the rotor exit.

A more detailed picture can be drawn when considering the circumferentially mass and time-averaged measured rms of the rotor relative total pressure. Figure 7 compares this parameter at rotor exit and the nominal injection rate for the three different geometries tested. The radial distributions confirm the trends found for the maximum rms values. However, the increase of the radial RMS distribution around the hub loss core due to the presence of the bubble (rotor B versus rotor A) is less significant than the increase of RMS when going from profiled to cylindrical end walls. Numerically, a mass-weighted integral of the rms distribution between 25% and 60% span shows a 15% increase due to the presence of the bubble (from A to B) and a 30% increase when the end walls become axisymmetric (from B to C) at the nominal injection rate. The benefit in terms of mass-weighted rms in the region of the hub passage vortex due to end wall profiling is about twice as big as the benefit gained when the bubble is suppressed. The mass-weighted integral of the experimental rms between 25% and 60% span increases by 50% when both beneficial effects are combined (from A to C). When considering an integral over one entire rotor pitch, the overall level of rms increases by 27% between rotors A and C.

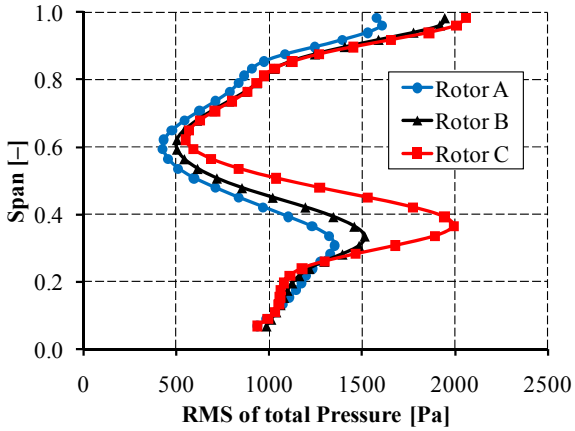

Figure 7. Radial distribution of circumferentially mass and time-averaged measured rms of the rotor relative total pressure $P_{t,rel}$ [Pa] at rotor exit and the nominal injection rate for the three different rotor geometries.

In the next paragraph, the dependency on the injection rate is analysed. Generally, the measured effect of injected purge flow on the rotor exit flow is intrinsically similar for all rotor geometries. Area plots of the measured rms in the rotor relative frame of reference are shown in Figure 8 for the highest and lowest injection rates and for rotor B. In the same manner as the geometrical modifications, only the hub vorticies (zone 1) are influenced by the addition of more purge flow, indicating where the injected purge flow migrates to at the rotor exit. The injected fluid interacts with the hub secondary flows, ending up in the core of the passage vortex, where it increases the unsteadiness. For instance, the measured peak rms value in the hub passage vortex increases by about 35% per percent of injected purge

flow for rotor B. The other secondary flow structures (zones 2 to 4) and the free steam region between the rotor wakes appear to remain unaffected. The measured peak rms values in the hub loss core increase with the addition of purge flow in a relatively linear manner (Figure 6). However, the sensitivity to purge flow is different between the rotor geometries. The sensitivity of peak nondeterministic unsteadiness is twice as high for rotor C compared to rotor A. The presence of end wall profiling and the suppression of the pressure side separation both clearly reduce the sensitivity of hub passage vortex unsteadiness to purge flow. These results are in line with the sensitivities found for the total-to-total efficiency (Figure 4).

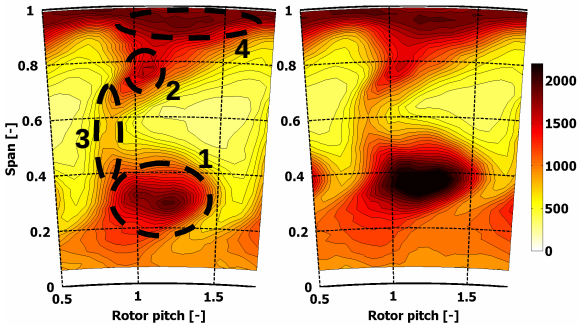

(a) IR=0.4% (b) IR=1.2%

Figure 8. Time-averaged area plot in rotor relative frame of reference at rotor exit for rotor B. The parameter is the experimental rms of the rotor relative total pressure $P_{t,rel}$ [Pa].

These findings are confirmed by the radial distribution of circumferentially mass and time-averaged experimental rms of the relative total pressure for different injection rates shown in Figure 9. A mass-weighted integral of the rms distribution between 25% and 60% span shows a 20% increase between lowest and nominal and between nominal and highest injection rates. The integral shows the same linear trend as the experimental peak rms. When considering an integral over one entire rotor pitch, the overall level of rms increases by 20% per percent of injected purge flow.

Considering the combined effects of injection rate and rotor geometry on the unsteadiness in the hub loss core shows that the beneficial effect of the end wall profiling can compensate for the increase of rms due to 0.8% additional purge flow (Figure 6). The suppression of the bubble again accounts for about 0.8% injected purge flow when operating without the bubble: rms for rotor B at IR=0.4% ≈ rms for rotor A at IR=1.2%.

In Figure 9 it can be seen that the measured modifications to the flow field caused by a variation of purge flow only reach a height of about 65% span at rotor exit. Assuming the centre of the hub passage vortex close to the location of maximum unsteadiness, the measurements show a radial migration of the hub loss core as a function of the injection rate (Figure 9). For higher injection rates the loss core penetrates the free stream region more.

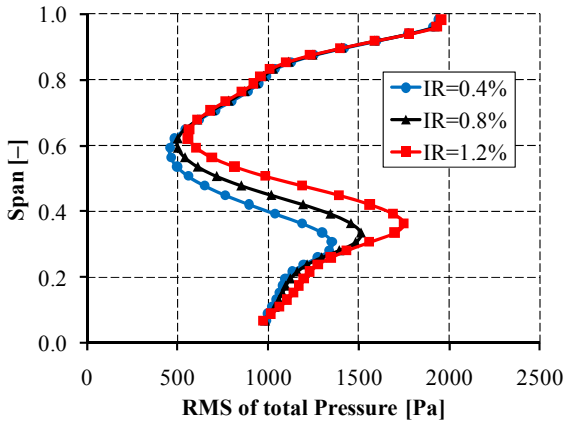

Figure 9. Radial distribution of circumferentially mass and time-averaged measured rms of the rotor relative total pressure $P_{t,rel}$ [Pa] for different injection rates. Results at the exit of rotor B are plotted.

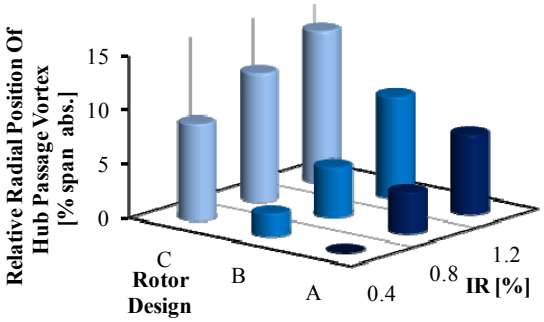

Figure 10. The bars indicate the relative span-wise position of the centre of the hub passage vortex with reference to the baseline rotor A at the lowest injection rate. The figure compares measurements from all nine investigated test cases (3 injection rates versus 3 rotor geometries) at rotor exit.

Figure 10 shows the relative radial position of the centre of the hub passage vortex in function of injection rate and rotor geometry. The reference is the loss core at the lowest radial position (21% span), which is measured at the minimum injection rate, end wall profiling and with no separation bubble (rotor A). In the test cases presented, the loss core migrates about 10% in span-wise direction per percent of injected purge flow for rotors A and B, following a linear trend with regard to the injection rate. With cylindrical end walls (rotor C) the sensitivity of radial migration to injected purge flow appears to be reduced to 7% span per percent of injected purge flow, however at a much higher overall span-wise

position. The absence of end wall profiling (rotor C) increases the radial penetration of the hub passage vortex by about 6% span for all experimentally investigated injection rates compared to rotor B. The suppression of the pressure side separation (rotor A) further reduces the radial position of the hub loss core by about 2% for all three levels of purge flow.

Figure 11 shows the time-averaged streamwise vorticity Ω_S at rotor exit in the rotor frame of reference for rotor A at the nominal injection rate. The two arrows indicate the footprint of the rotor hub and tip passage vorticies. The streamwise vorticity is the scalar product of the vorticity vector and the primary flow vector. The required axial gradients are approximated using a frozen flow structure assumption. The detailed approach and calculations can be found in Schuepbach et al. [16].

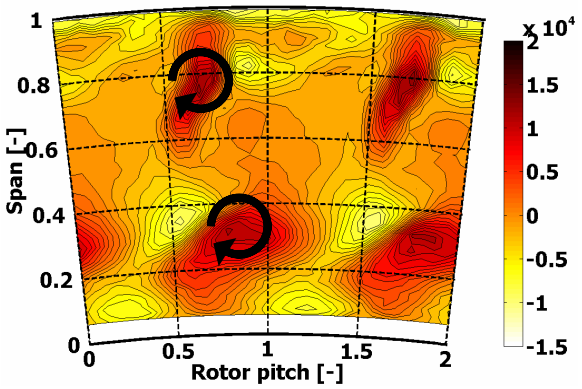

Figure 11. Time-averaged area plot in rotor relative frame of reference at rotor exit for rotor A at nominal injection rate (IR=0.8%).The parameter is the streamwise vorticity Ω_S [1/s].

As for the relative total pressure RMS distributions the main difference in streamwise vorticity between the nine investigated test cases (three injection rates versus three rotor geometries) is found in the hub loss core (zone 1 in Figure 5) . The vorticity distributions in the rest of the measured flow field appear to be little affected by the level of purge flow and the rotor geometry. In order to compare the hub passage vortical structures for different injection rates, the circulation has been calculated by integrating the streamwise vorticity over the area affected by the hub passage loss core. The streamwise vorticity inside an iso-contour of zero vorticity has been considered. Figure 12 compares the circulation of the hub passage vortex between all test cases, based on measurements and CFD computations. For all geometries the addition of purge flow increases the circulation in the hub loss core. The lowest values for the circulation integral were found for baseline rotor A. Experimentally, Rotor C with axisymmetric end walls shows a 30% higher value at the high injection rate compared to the baseline rotor A at the low injection rate (7.3 m^2/s), which was chosen as a reference in Figure 12. The experimental variation of the circulation integral is three times weaker than predicted by the simulations. The reasons for this are not fully understood and are currently under investigation. Both the presence of a pressure side separation and the removal of the end wall profiling increase the level of measured and predicted circulation in the hub passage vortex, especially at higher injection rates. At the lowest injection rate the measured circulation decreases from rotor B to rotor C. The end wall profiling was designed at the nominal injection rate, but appears to have an adverse effect at lower injection rates than assumed in the design. The sensitivity of the measured and predicted circulation to purge flow for rotor C with cylindrical end walls is about twice as high (20% per percent of injected purge flow) as for rotors A and B. The end wall profiling present for rotors A and B successfully reduces the sensitivity of circulation and loss to purge flow in the hub passage vortex.

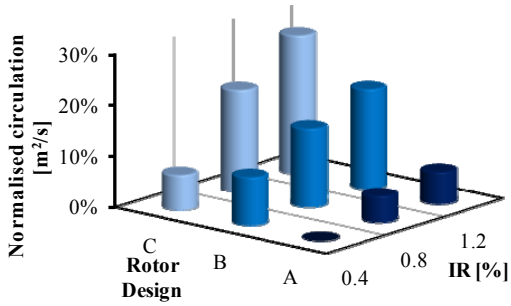

(a) Experiment

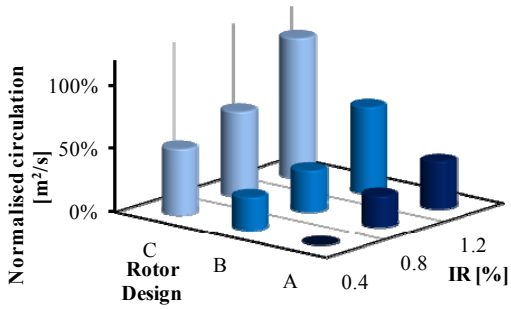

(b) Simulation

Figure 12. The bars indicate relative circulation of the hub passage vortex with reference to the baseline rotor A at the minimum injection rate. The figure compares measurements from all nine investigated test cases (3 injection rates versus 3 rotor geometries) at rotor exit.

Figure 13 shows the circumferentially mass and time-averaged streamwise vorticity plots for the three rotor geometries at the nominal injection rate. The streamwise vorticity for rotor C with cylindrical end

walls is clearly higher when compared to rotors A and B with profiled end walls. The difference in circumferentially mass-averaged Ω_S between rotors A and B is relatively small in comparison. In consequence the end wall profiling seems to have the main impact on the vorticity at rotor exit. The high streamwise vorticity is concentrated in a limited span-wise region. The suppression of the bubble (between rotors A and B) has a minor effect on the measured streamwise vorticity. However the circulation and the peak streamwise vorticity are each about 10% lower for the baseline rotor A compared to rotor B. Therefore the presence of the pressure side bubble on rotor B seems to spatially concentrate the high vorticity fluid more than is the case for rotor A without the bubble, increasing the peak vorticity and circulation. The mass-weighted average also increases in the area, but not to the same extent.

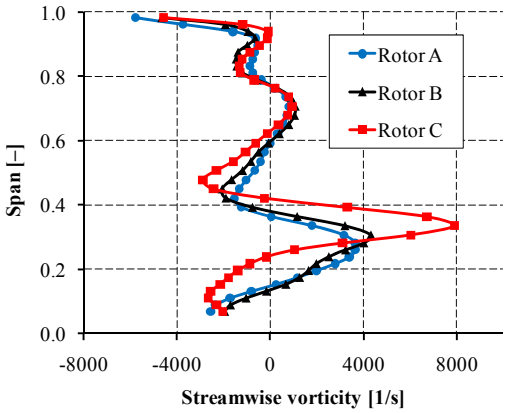

Figure 13. Radial distribution of circumferentially mass and time-averaged streamwise vorticity Ω_S [1/s] at rotor exit for the three rotor geometries at IR=0.8%.

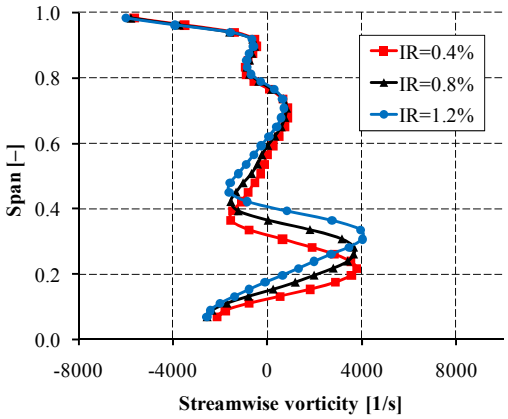

Figure 14. Radial distribution of circumferentially mass and time-averaged streamwise vorticity Ω_S [1/s] at rotor exit for baseline rotor A at different injection rates.

The streamwise vorticity distributions in Figure 13 show the same 10% of span-wise radial migration between rotors A and C as observed for the relative total pressure distributions. Figure 14 shows the effect of injected purge flow on the radial distribution of streamwise vorticity for the baseline rotor A. The circumferentially mass and time-averaged radial distributions in Figure 14 show that the time-averaged vorticity in the hub loss core does not increase with purge flow. However additional purge flow affects the circulation of the hub passage vortex. It slightly increases by 8% per percent of injected purge flow (Figure 12). As shown in Figure 9, the purge flow has no influence on the flow field above 65% span. Above this radial position the measurements show very good consistency.

Conclusions

The results of a combined experimental and computational investigation covering nine test cases are presented in this paper. Three shrouded low-pressure rotor geometries with profiled hub and tip end walls for two of the rotors were studied at three levels of rim seal purge flow (0.4%, 0.8% and 1.2%). The purge flow migration, transport and interaction mechanisms with the turbine main flow containing a rotor pressure side separation for two of the rotor geometries were studied and quantified. The time-resolved measurements are very consistent between the test cases and were made in a one-and-half stage shrouded model axial turbine with profiled NGV using a fast response aerodynamic probe (FRAP).

The rotor with profiled end walls and without pressure side separation showed the highest efficiency for all purge flow levels. The total-to-total efficiency was reduced by 0.3% due to the presence of a separated pressure side and by another 0.75% on average when the rotor end wall profiling was removed. For all rotor geometries the efficiency decreased linearly with the addition of purge flow. The end wall profiling reduced the sensitivity of efficiency to purge flow twice as much (20% per percent of injected purge flow) as the suppression of the pressure side bubble. The rotor end wall design presented is able to compensate for the efficiency deficit due to 0.6% of additional purge flow.

The purge flow was found to strongly interact with the rotor hub passage vortex and to affect its radial position. For all geometries, the radial position of the hub loss core increased by about 10% span per percent of injected purge flow. The end wall profiling and the suppression of the pressure side bubble both reduced the overall span-wise position of the loss core.

In the same manner, the additional purge flow increases the maximum root mean square values of the measured relative total pressure random part and

the circulation in the hub loss core for all rotors tested. However the sensitivities of theses parameters to purge flow depend on the rotor geometry. Both, the end wall profiling and the suppression of the pressure side bubble reduce the sensitivity to purge flow by approximately the same amount.

In contrast, the streamwise vorticity appears to be little affected by purge flow and the pressure side bubble. However the end wall profiling causes a 50% reduction of peak streamwise vorticity in the hub loss core. Purge flow and the suppression of the bubble cause a significant increase in turbulence in the hub loss core but not much of an increase in streamwise vorticity.

Acknowledgement

The work leading to the results presented in this paper was carried out within the joint industrial and academic research program that is part of the ”Luftfahrtforschungsprogramm LuFo4” supported by the German Federal Ministry of Economics and Technology.

References

[1] Chew, J. W., Dadkhah, S., and Turner, A. B., 1992. “Rim Sealing of Rotor-Stator Wheelspaces in the Absence of External Flow”. Journal of Turbomachinery-Transactions of the ASME, 114(2), pp. 433–438.

[2] Dadkhah, S., Turner, A. B., and Chew, J. W., 1992. “Performance of Radial Clearance Rim Seals in Upstream and Downstream Rotor-Stator Wheelspaces”. Journal of Turbomachinery-Transactions of the ASME, 114(2), pp. 439–445.

[3] Kobayashi, N., Matsumato, M., and Shizuya, M., 1984. “An Experimental Investigation of a Gas Turbine Disk Cooling System”. Journal of Engineering for Gas Turbines and Power-Transactions of the ASME, 106(1), pp. 136– 141.

[4] McLean, C., Camci, C., and Glezer, B., 2001. “Mainstream Aerodynamic Effects Due to Wheelspace Coolant Injection in a High-Pressure Turbine Stage: Part II – Aerodynamic Measurements in the Rotational Frame”. Journal of Turbomachinery-Transactions of the ASME, 123(4), pp. 697–703.

[5] Ong, J. H. P., Miller, R. J., and Uchida, S., 2006. “The Effect of Coolant Injection on the Endwall Flow of a High Pressure Turbine”. In ASME Turbo Expo, GT2006-91060.

[6] Paniagua, G., Denos, R., and Almeida, S., 2004. “Effect of the Hub Endwall Cavity Flow on the Flow-Field of a Transonic High-Pressure Turbine”. Journal of Turbomachinery-12 Copyright c 2011 by ASME Transactions of the ASME, 126(4), pp. 578–586.

[7] Reid, K., Denton, J., Pullan, G., Curtis, E., and Longley, J., 2006. “The Effect of Stator-Rotor Hub Sealing Flow on the Mainstream Aerodynamics of a Turbine”. In ASME Turbo Expo, GT2006-90838.

[8] Schuepbach, P., Rose, M. G., Abhari, R. S., and Gier, J., 2011. “Influence of Rim Seal Flow on the Performance of an Endwall-Profiled Axial Turbine”. Journal of Turbomachinery- Transactions of the ASME, 133(1).

[9] Riollet, G., 1970. “Curved Channels Through which a Gas or Vapor Flows”. United States Patent 3529631.

[10] Rose, M. G., 1994. “Non-axisymmetric Endwall Profiling in the HP NGVs of an Axial Flow Gas Turbine”. In ASME Turbo Expo, 94-GT-249.

[11] Hartland, J. C., Gregory-Smith, D. G., Harvey, N. W., and Rose, M. G., 2000. “Non-axisymmetric Turbine End Wall Design: Part II - Experimental Validation”. Journal of Turbomachinery-Transactions of the ASME, 122(2), pp. 286–293.

[12] Ingram, G. L., Gregory-Smith, D. G., Rose, M. G., Harvey, N. W., and Brennan, G., 2002. “The Effect of End-Wall Profiling on Secondary Flow and Loss Development in a Turbine Cascade”. In ASME Turbo Expo, GT2002-30339.

[13] Brennan, G., Harvey, N.W., Rose, M. G., Fomison, N., and Taylor, M. D., 2003. “Improving the Efficiency of the Trent 500 HP Turbine Using Non-Axisymmetric End Walls: Part I:Turbine Design”. Journal of Turbomachinery-Transactions of the ASME, 125(3), pp. 497–504.

[14] Rose, M. G., Harvey, N. W., Seaman, P., Newman, D. A., and McManus, D., 2001. “Improving the Efficiency of the Trent 500 HP Turbine Using Non-Axisymmetric End Walls: Part II: Experimental Validation”. In ASME Turbo Expo, GT2001-0505.

[15] Praisner, T. J., Allen-Bradley, E., Grover, E. A., Knezevici, D. C., and Sjolander, S. A., 2007. “Application of Non-Axisymmetric Endwall Contouring to Conventional and High-Lift Turbine Airfoils”. In ASME Turbo Expo, GT2007-27579, Vol. 6.

[16] Schuepbach, P., Rose, M. G., Abhari, R. S., Germain, T., Raab, I., and Gier, J., 2008. “Improving Efficiency of a High-Work Turbine using Non-axisymmetric Endwalls. Part II: Time-resolved Flow Physics”. In ASME Turbo Expo, GT2008-50470.

[17] Germain, T., Nagel, M., Raab, I., Schuepbach, P., Rose, M. G., and Abhari, R. S., 2010. “Improving Efficiency of a High-Work Turbine Using Non-Axisymmetric Endwalls. Part I: Endwall Design and Performance”. Journal of Turbomachinery-Transactions of the ASME, 132(2).

[18] Brear, M. J., Hodson, H., and Harvey, N., 2002. “Pressure Surface Separations in Low-Pressure Turbines – Part 1: Midspan Behaviour”. Journal of Turbomachinery- Transactions of the ASME, 124(3), pp. 393–401.

[19] Yamamoto, A., and Nouse, H., 1988. “Effects of Incidence on Three-Dimensional Flows in a Linear Turbine Cascade”. Journal of Turbomachinery of the ASME, 110(4), pp. 486–496.

[20] Hodson, H., and Dominy, R., 1987. “The Off-Design Performance of a Low-Pressure Turbine Cascade”. Journal of Turbomachinery of the ASME, 109(2), pp. 201–209.

[21] Brear, M. J., Hodson, H., Gonzalez, P., and Harvey, N., 2002. “Pressure Surface Separations in Low-Pressure Turbines - Part 2: Interactions with the Secondary Flow”. Journal of Turbomachinery of the ASME, 124(3), pp. 402–409.

[22] Kupferschmied, P., Kopperl, O., Gizzi, W. P., and Gyarmathy, G., 2000. “Time-Resolved Flow Measurements with Fast Aerodynamic Probes in Turbomachinery”. Meas. Sci. Technol., 11, pp. 1036–1054.

[23] Pfau, A., Schlienger, J., Kalfas, A. I., and Abhari, R. S.,2003. “Unsteady 3-Dimensional Flow Measurement Using a Miniature Virtual 4-Sensor Fast Response Aerodynamic Probe (FRAP)”. In ASME Turbo Expo, GT2003-38128.

[24] Jenny, P., Abhari, R. S., Rose, M. G., Brettschneider, M. and Gier, J., 2011. “A Low Pressure Turbine with Profiled End Walls and Purge Flow Operating with a Pressure Side Bubble”. In ASME Turbo Expo, GT2011-46309

[25] Germain, T., Nagel, M., and Baier, R.-D., 2007. “Visualisation and Quantification of Secondary Flows: Application to Turbine Bladings with 3D-Endwalls”. In Proceedings of the ISAIF, Lyon.